2010 Human Powered Vehicle Competition
Central Connecticut State University
New Britain, CT

VEHICLE #3

Design Report

Olin College Human Powered Vehicle

Bucephalus

Franklin W. Olin College of Engineering

Team Leaders: Jacob Izraelevitz and Alex Niswander

Casey Canfield, Andrew Carmedelle, Elsa Culler, Pam Darvirris, Geeta Gubba, Carl Herrmann, Eric Jones, Ariel Leigh, Meghan Murray, Heidi Nafis, John Rosenwinkel, Travis Schuh, Ben Smith, Sasha Sproch, David Stamp, Gray Thomas

Table of Contents

Abstract
The Olin College Human Powered Vehicle Team is returning this year for its fourth ASME HPV Challenge. This year, our main goals are improved efficiency, ergonomics, and ridability. Once again, we built a prototype vehicle first before beginning fabrication of the competition vehicle in order to guide our design and analysis. We make it our goal every year to design the HPV so that it can be configured to fit any member of the team, so this required a substantial design change.

As a result of our experimentation with the prototype, we implemented several major changes to this year's competition vehicle, *Bucephalus*, compared to last year's vehicle, *Helios*:

1. We decided to return to front wheel drive to decrease drivetrain footprint. We found that improved manufacturing techniques and increased adjustability in the implementation dramatically improved overall reliability.
2. We also developed an innovative fairing fabrication technique. Rather than building traditional molds for the fiberglass layup, we sewed a "sock" in the shape of our fairing and inflated it with a large weather balloon. While this technique is less precise, it resulted in a smooth approximation of our designed shape.
3. The seat is designed with adjustability in two dimensions. In addition to sliding backwards and forwards, the seat angle is discretely adjustable to four positions. This has the added benefit of simplifying fairing construction since it allows us to keep riders' eye level relatively constant.
4. Lastly, we implemented an innovative below-seat steering geometry. Without sacrificing maneuverability, this geometry improves the ergonomics for all riders.

Overall, we are proud of the results of our innovative design efforts and we hope these changes will help us improve our competition performance.

Design and Innovation
We began our design process with a group brainstorming session emphasizing radical changes that could be made to improve the vehicle. From this starting point, we built a prototype vehicle that served as a testing platform for our ideas. This iterative process of building two vehicles allowed us to experiment with innovative designs before construction of our competition vehicle.

Frame Design
For our initial prototype, we decided to build on our growing experience and push ourselves to experiment. As a result, we decided to return to front wheel drive and try below-seat steering. In addition, we evaluated our frame using several comparative metrics, assigning each option a numerical rating according to how well it fulfilled the metric. This method weights each criterion equally and is somewhat arbitrary; the results should be taken lightly but can be used to guide the design process. Table 1 shows a comparison of this year's prototype with our two previous vehicles and uses a conventional bicycle as a control. The criteria we used for comparison were: aerodynamics of fairing (frontal area), ergonomics and rider comfort, stability and rider confidence in maneuverability, team familiarity with frame type, and innovation of frame geometry.

DESIGN MATRIX				
Criteria	***Vega* (2008)**	***Helios* (2009)**	**Prototype (2010)**	**Standard Bicycle**
Aerodynamics	4	2	3	1
Ergonomics	1	2	3	4
Stability	1	3	2	4
Experience	3	4	2	3
Innovation	3	2	4	1
TOTALS	**12**	**13**	**14**	**13**

Table 1. Design Matrix for 2010 Prototype – Note that a rating of 1 is worst and 4 is the best.

While this year's prototype is our most innovative vehicle, it does not score the highest in any other metric. This year's vehicle is an improvement from last year in terms of aerodynamics and ergonomics – two factors which we expect to strongly factor into competition performance. Aerodynamics is improved by a lower seat angle and the new steering geometry is much more ergonomic. The decreased stability and familiarity is a result of the new steering geometry, which our team is less familiar with riding and fabricating. However, this year's prototype still emerged as the optimal design with which to move forward.

In addition we designed our frame for ease of manufacture to simplify the welding process. In prototype fabrication we noted that minimizing the number of joints and welds greatly improved the in-plane alignment of the frame members. As a result our drivetrain experiences fewer chain derailment issues, a great improvement over previous years. Additionally we made a few modifications to the prototype geometry to further improve ridability and reduce frontal area.

As shown in Figure 1b, we increased the angle between tubes I and II so that a sixteen-inch wheel would fit the contour of the frame. We had initially built the prototype vehicle with a 20in front wheel which had pedal interference issues that required reducing the wheel size. To keep a low vehicle profile and avoid any possible interference issues, we selected a 16in front wheel for the final design, enabling us to lower tube I, bringing our feet out of our vision path. Also, we adjusted the angle of the main frame tube (tube III) to angle down slightly towards the rear of the vehicle, compared to the horizontal frame tube in our prototype. This slight angle also helps us maintain a low profile while accommodating riders of various sizes as tall riders will sit farther back, and thus slightly below, shorter riders, reducing effective height of taller riders.

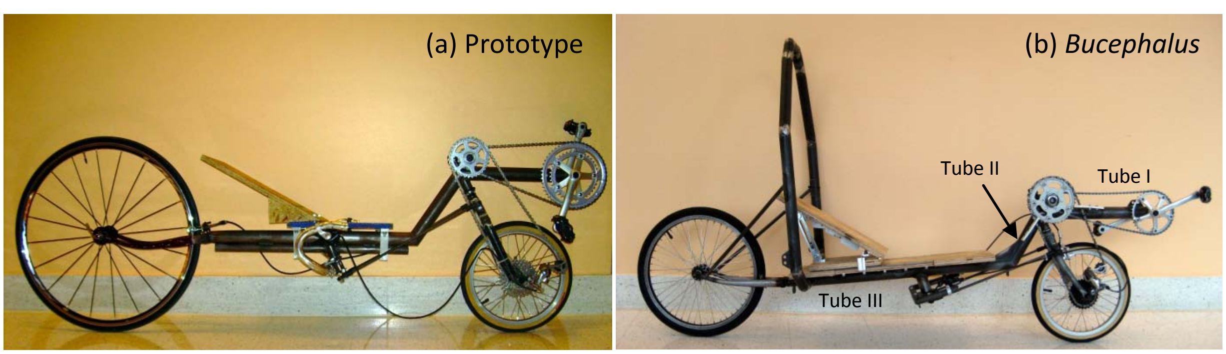

Figure 1: Comparison of prototype (a) and competition (b) frame geometries – Note optimized frame geometry of *Bucephalus*.

Steering Design

In past years, we have positioned the steering handlebars directly in front of the rider's chest. This steering position has the advantage of being similar enough to a normal bicycle that it decreased the learning curve for riding our vehicle. It is also remarkably space efficient, taking up existing room in the fairing between the rider's chest and knees.

However, while taking ergonomic measurements, we discovered that our tallest team member's knees intersect our shortest rider's chest when riders were seated on the vehicle. It was highly difficult to place the steering mechanism in a single position that would be ergonomically sound for our entire rider range. Our four-bar linkage mechanism for steering control made an adjustable steering position highly complex, so we decided to move the entire handlebar system beneath the rider's seat as shown in Figure 2. This kind of steering arrangement has been successfully implemented by previous recumbent bike designers.

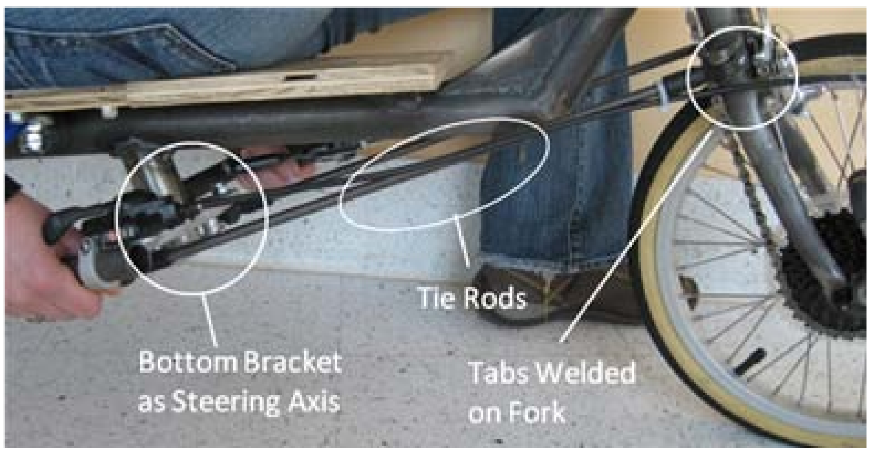

Figure 2: Our below-seat steering system. The handlebars rotate about an axis parallel to the fork, and actuate the fork through two tie rods.

Our design consists of a bottom bracket welded midway down the main support tube, with the bracket axis parallel to the fork axis. The handlebars rotate about the bottom bracket axle and actuate the fork through a four-bar linkage mechanism. We implemented this system on this year's prototype and found the steering placement accessible to all of our riders. We used a set of road bike handlebars to allow for easy experimentation in hand placement. After significant road testing, we found that we were comfortable with short handlebars.

Placing the steering mechanism below the rider places the point of rotation for the handlebars much closer to the frame, eliminating the need for extensive, cantilevered supports. Last year's *Helios* had a mechanically sloppy steering linkage as a result of handlebar support with a single radial bearing at the end of a long unsupported tube. The bottom bracket used this year contains two axially displaced bearings and is mounted directly to the frame, improving moment load support. As expected, we found this new steering design was substantially stiffer and exhibiting lower backlash than *Helios*'s.

Seat Design

We used a Design for Usability focus for the seat. Our primary design goal for the seat was to be able to easily and quickly adjust the seat position between the shortest and tallest rider positions while having a seat that was rigid enough to support the rider while they pedaled.

The seat on *Helios* had several primary problems, most notably difficult seat adjustment and poor construction. For the 2010 prototype, we prioritized drivetrain design, neglecting seat design experimentation. We decided to fabricate a seat with a shallow 30° angle, to minimize frontal area. This seat design confirmed previous observations of design issues, as riders noted difficulty with adjustment and some disliked the shallow seat angle.

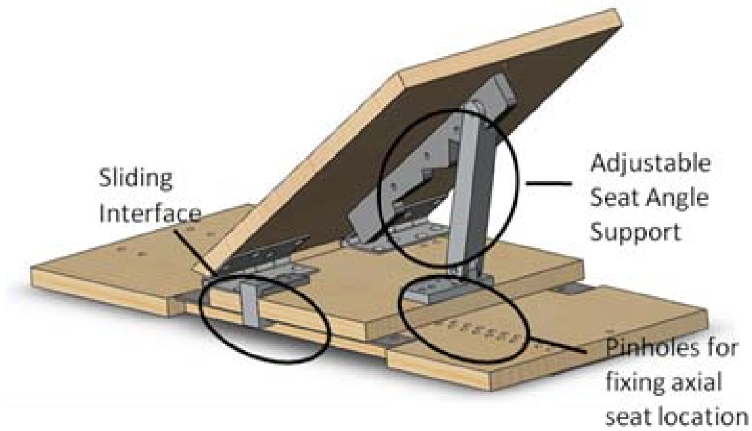

Figure 3: Solid model of seat and adjustment mechanisms – The seat base is bolted to the frame, the seat back glides on rails, and both seat location and angle are easily adjustable to discrete positions.

To address these issues, we developed a seat design with adjustable seat position and seat back angle as shown in Figure 3. The fixed seat bottom allows us to create a rigid platform for the seat while avoiding conflict with the below-seat steering. To adjust the seat position, the seat back slides relative to the seat bottom and is then locked in place by a pin. This has the advantage of moving the adjustment mechanism to the top side of the seat where it is easily accessible and simplifying it to a single pin. The pin system also creates a discrete set of holes, making it easier to identify and mark the appropriate seat positions for different riders.

We initially reduced the seat angle because doing so lowers the profile of the tallest riders, but this comes at the cost of rider stability. Because only shorter riders had issues with low seat angles and short riders do not define the fairing profile, we could raise the seat angle without sacrificing frontal area. The adjustable seat back angle also has the added benefit of increasing the uniformity of eye level height since taller riders are able to lean further back than shorter riders. This seat design has greatly improved adjustability and ergonomics for our riders.

Drivetrain Design

At the beginning of the year we set out to build a drivetrain that was both reliable and efficient. *Helios* used a rear wheel drive configuration with two stages, a reduction from the drive chain ring to an interchange and a reduction from the interchange to a cassette on the rear wheel. This drive allowed for extreme turning radiuses, even while pedaling. However, the rear wheel drivetrain had reliability issues, chain path interference problems with the front wheel and seat, and unnecessary bulkiness due to chain routing to the rear wheel. Based on this experience, we wanted to focus on making our drivetrain more reliable and compact without sacrificing efficiency.

From these design goals, we decided to prototype a front wheel drivetrain with a two stage reduction. Although previous attempts at front wheel drive had proved unreliable, we had reason to believe we could improve on these designs with our increased experience. From this prototype we found the drivetrain to be reliable without significant optimization. Even without any chain guides, the chains did not derail during normal riding. The chain occasionally fell off at the large sprocket of the interchange while making sharp turns. However, after adding a chain guide, the chain rarely fell off even when turning and riding over bumpy grounds. This prototype gave us confidence in our ability to develop a reliable front wheel drive system.

On the prototype we were able to size a combination of sprockets and chain length for the first drivetrain stage that required no external tensioning. To provide greater freedom in gear selection, we generated a variety of chain tensioning concepts. These included adding an eccentric bottom bracket, and moving the interchange with either a slot and cam system or a slot and spacer system. We chose the slot and spacer system as shown in Figure 5, because it had the best combination of price and manufacturability.

Figure 4: Front wheel drivetrain on *Bucephalus* – Note the two stage reduction with no chain tensioner on first stage.

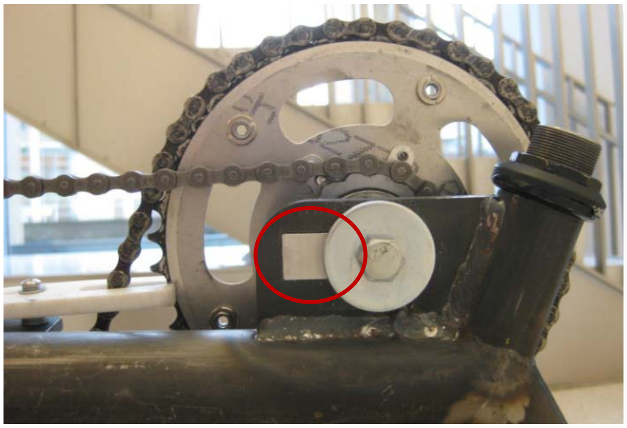

Figure 5: Tensioning system at the interchange – The first chain reduction is tensioned with aluminum insert (circled).

Our target top speed for the bike is approximately 49mph. In order to pick gear ratios, we created a spreadsheet that predicts the bike speed given the sprocket sizes, the wheel size, and rider cadences. We estimated a high cadence of 120rpm, a mid/target cadence of 100rpm, and a low cadence of 80rpm. We chose to use a standard 8-speed cassette and a 42T large sprocket at the interchange in order to clear the fork. Based on these constraints, we picked a ratio for the first reduction to achieve our design goal. Our final top speed at max cadence in the highest gear is predicted to be at 49mph and our slowest speed at low cadence in the lowest gear is predicted to be at 14mph.

CRANKSET	38	teeth
INTERCHANGE 1	15	teeth
INTERCHANGE 2	42	teeth
WHEEL DIA.	15.5	in
LOW RPM	80	rpm
MID RPM	100	rpm
HIGH RPM	120	rpm

CASSETTE	RATIO	LOW SPEED	MID SPEED	HIGH SPEED
28 T	3.80	**14.02 mph**	17.52 mph	21.03 mph
26 T	4.09	15.10 mph	18.87 mph	22.64 mph
23 T	4.63	17.07 mph	21.33 mph	25.60 mph
20 T	5.32	19.63 mph	24.53 mph	29.44 mph
18 T	5.91	21.81 mph	27.26 mph	32.71 mph
16 T	6.65	24.53 mph	30.66 mph	36.80 mph
14 T	7.60	28.04 mph	35.05 mph	42.05 mph
12 T	8.87	32.71 mph	40.89 mph	**49.06 mph**

Table 2: Gear Ratio Design – Note the low speed of 14mph and high of 49mph.

Roll Bar Design

The most important factors in the roll bar design are geometry and strength. The roll bar's main function is to protect the rider from injury in the event of a crash. As far as geometry was concerned, we wanted our roll bar to present as small a profile as possible without compromising the comfort of our riders so that we could minimize *Bucephalus'*s frontal area. In order to account for every rider on our team, we used measurements taken from our largest and smallest riders on a mockup of the vehicle. We sat helmeted riders on *Bucephalus* during its construction against a consistent background and photographed them, overlaying the photos in Adobe Photoshop to compare head and shoulder positions (Figure 6). In addition to these photos, we also collected specific measurements, such as foot, knee, hip, eye, and top of head locations. With these measurements, we identified the shape occupied by the rider and used those dimensions to construct a fairing and roll bar geometry that accommodated everyone.

Figure 6: Overlay of the tallest and shortest riders on *Bucephalus* – The vertical line is a measuring tool used for scaling the picture in CAD. Notice how rider eye level remains roughly constant despite substantially different rider positions and sizes.

We used a cardboard mockup of potential roll bar designs to evaluate rider comfort and fit. Rider entry and exit necessitated roll bar placement near the rear of the vehicle. For ease of manufacture, we mounted the roll bar perpendicular to the main tube, angling it relative to the vertical plane. The roll bar is fabricated from the same steel tubing used in the construction of the frame, due to its high tensile strength, toughness, and ease of system integration. Our FEA found an undesirably high stress at the roll bar's intersection with the main frame tube. To remedy this, we added triangulating members to support the moment load (refer to Roll Bar Analysis section), producing the final design shown in Figure 7.

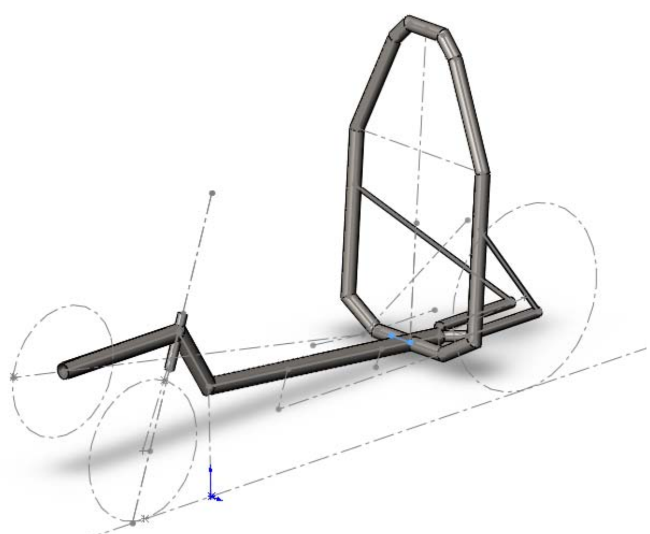

Figure 7: Final roll bar design.

Fairing Shape Design

Fairing design is a trade-off between drag, ergonomics, crash safety, and visibility. By defining the shape limitations due to the vehicle and rider in terms of perpendicular cross-sections, we were able to systematically design a fairing of minimal frontal area. Using our rider measurements and photos, we were able to develop top and bottom curves for the fairing as shown in Figure 8. We chose top and bottom curves to minimize unused space while providing a smooth curve, minimizing frontal area, and accounting for measurement errors of ±0.5in. We designed the fairing to intersect the roll bar at its corners to provide a close fit. The nose and tailbox were both designed for smooth aerodynamic performance while keeping vehicle length within manageable limits.

Figure 8: Top and bottom curves wrapping around riders.

Next, we identified six key locations to define the shape of the fairing and fit the rider, including around the pedal path, the transition to the canopy, and the roll bar. We defined each cross section as a symmetric spline with six defining points: two on the central plane, and two mirrored pairs to be later used for three dimensional guide curves. This technique ensured manufacturability by preventing the use of fairing curvatures that would be difficult to fill with a balloon. The only exception was the high curvature region at the tail which we planned to define separately. The fairing shape was extrapolated by a loft between the cross-sections using four guide curves between the spline points of each cross-section.

Finally, we designed for window and door placement. In the past, we have experimented with thermoformed windows to achieve complex geometries; however, the thermoformed plastic reduces visibility to an unacceptable level. Instead, we chose to use clear PETG plastic bent in a single dimension for our window and modeled a window based on this simple bending constraint. We adjusted the window's shape to maximize visibility for various riders. Imprecision associated with our fabrication method will need to be accounted for in the final implementation. For rider entry and exit, we intend to cut the fairing post fabrication into nosecone, bottom, and top sections and have not yet finalized the shapes. Figure 9 shows the final fairing shape.

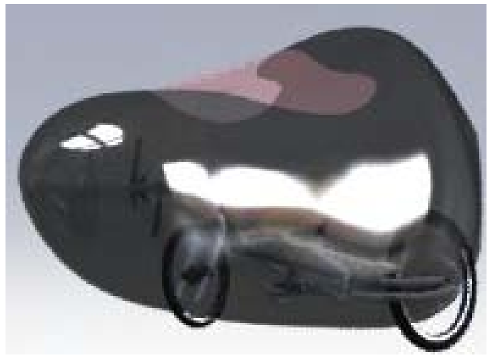

Figure 9: Final fairing shape with window.

Fairing Manufacture Process Design

Fiber-reinforced polymers possess attractive material properties for fairing design. They provide a high strength-to-weight ratio, and if prepared in only one or two layers, the resulting structure retains some flexibility that allows for small deformations and modifications. As is standard practice, we have chosen to fabricate a full fairing made of fiberglass epoxy composite matrix.

However, the major challenge of using fiber-reinforced polymer composite is the creation of the mold. In previous years, we have made male molds out of blue foam. However, given our lack of CNC capabilities for large objects, manufacturing a full fairing mold required an unacceptably high investment of time, labor, and money. Last year, we avoided mold construction by laying fiberglass on both sides of a 1" thick cardboard ribbing structure. This cardboard construction technique allowed us to make an inexpensive fairing, however, the final product contained surface imperfections where the fiberglass deformed between cardboard ribs.

This year we developed an innovative, low-cost technique to produce a high-quality fairing. The method involves creating a fabric "sock" in the shape of the inside of the fairing, applying uniform pressure to the inside of the sock by means of a weather balloon, and laying up either directly onto the sock or onto a layer of mold release. The main advantage of this method is cost; the mold cost less than $100 and forty man-hours of work to create. Though this method is not as precise as a foam-based mold, the monetary savings and ease of manufacture outweigh this loss of precision.

Mold Manufacture

SolidWorks, our preferred CAD software, does not support unfolding 3D objects into flat cutouts except in sheet metal parts. Converting our fairing to SolidWorks' sheet metal format proved ineffective, so we used a trial version of Lamina, a relatively new software package to convert our fairing design into a two dimensional fabric pattern. Using the shapes output by this program, we sewed the cutouts into two mold "socks", front and rear, because of our balloons' limited size. The rear taper of the fairing did not inflate properly, as expected, so we made an inner cavity for the balloon and filled the taper section manually with stuffing.

Figure 10. Fully inflated front-half mold.

Layup Technique

Given the inflated fabric, we wrapped the entire mold in saran wrap, a suggestion given to us by a local fiberglass professional [3]. The wrap acts as a mold release but also adheres well to the wet epoxy, allowing us to lay up the entire first layer at once, even on the underside. After curing this first layer, the fairing was highly flexible. The cloth "sock" only constrains the mold's surface area, not its shape, which we need to correct after the initial layup. Constraining the fairing with cardboard scaffolding around the outside of the shape, we laid up Coroplast ribs inside the fairing to hold it to the intended shape. Two more fiberglass layers on the outside will complete the fairing.

Analysis

Frame Analysis

We began frame analysis by determining the center of mass of several different riders in relation to the vehicle. We then created a mass-weighted average location for the center of mass. Our method consisted of placing a scale under each wheel of the vehicle and weighing each rider as they sat in their preferred riding position, first on a horizontal surface and then with the front wheel elevated 18in above the rear. Taking these values, we then wrote a script in MATLAB that calculates the center of mass location of each rider and the weighted average location.

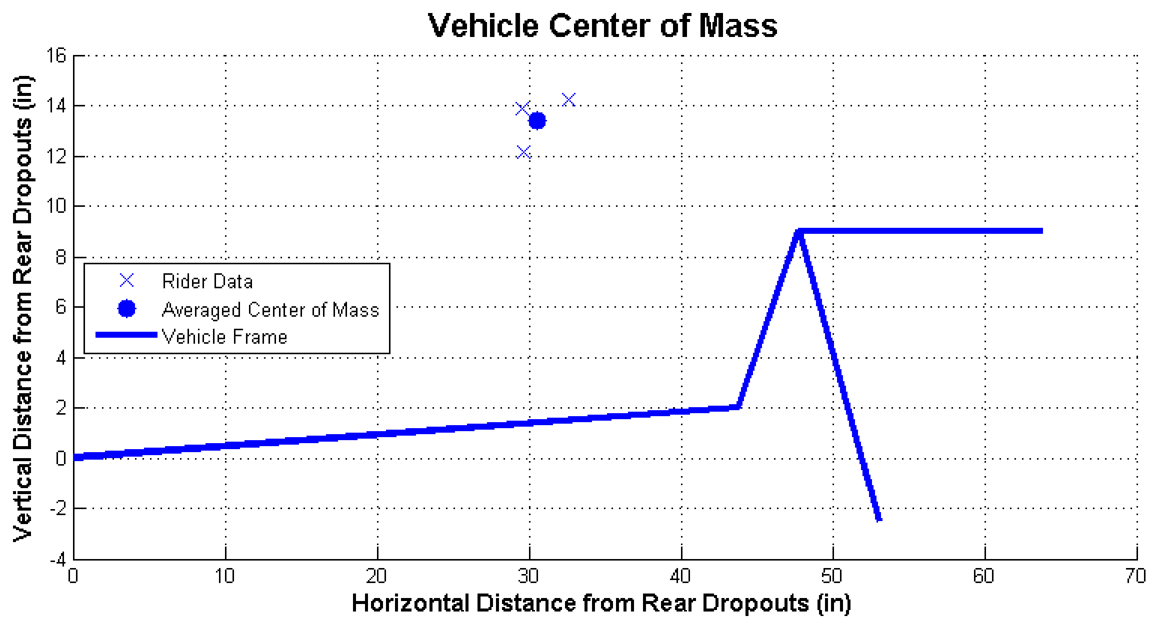

Figure 11: Center of mass data and calculated average – The vehicle center of mass was roughly constant between riders and was used to locate vertical and braking loads on the frame.

Assuming that gravity is the only vertical acceleration acting on the vehicle, we know maximum braking (with both wheels remaining in contact with the ground) occurs when the moment about the front wheel's contact point due to the rider's mass is exactly balanced by the moment due to the force of the rider's deceleration. Any more braking force and the vehicle would start to tip over forward. Based on the angle between the center of gravity and the front wheel's ground contact point, the maximum braking acceleration is approximately 0.95*g*.

After determining the location of the center of mass of our riders, we decided on a worst-case loading scenario for finite element analysis. We assumed a maximum rider weight of 200lbs and acceleration in two directions. A 3*g* bump is an industry standard [2] for worst case vertical acceleration. We verified that this acceleration (see Accelerometer Testing Section) is well in excess of anything we expect to see during practice or competition with our vehicle. We also assumed a 1*g* horizontal braking acceleration, approximately the maximum deceleration our vehicle can achieve.

Based on our rider weight, these accelerations give an overall load on the frame of 600lbf vertically downward and 200lbf forward. This loading was applied to the frame in ANSYS as a remote force. The front of the vehicle was fully constrained in translation at the head tube with a remote displacement constraint located at the front dropout. This process of fixing the front axle is standard industry practice [4]. The frame was additionally constrained in translation with another remote displacement constraint at the rear dropouts, except in the vehicle's axial direction, allowing the frame to flex downward while keeping both wheel axles fixed distances from the ground.

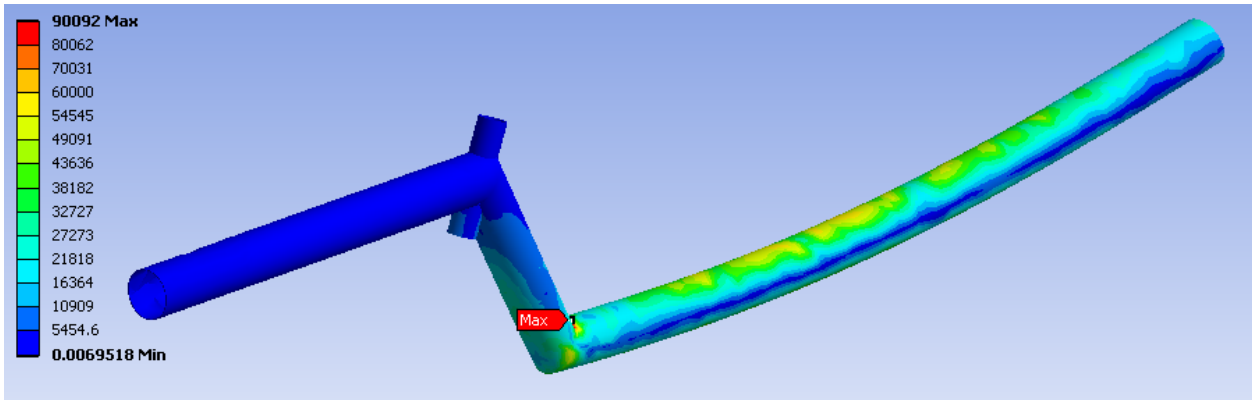

Figure 12: Equivalent stress distribution – Worst case loads of 600lbf downward and 200lbf forward were applied (stress values given in psi).

Our analysis, as seen in Figure 12, shows that the von Mises stress is well below the yield stress for our 4130 steel tube (approximately 60ksi). Stress along the top and bottom of the main tube approaches this value. Given that this is a worst case simulation and the predicted values do not exceed the yield stress, there are no points of concern save one stress concentration at the primary frame joint, highlighted in Figure 13. This concentration is extremely localized and is an artifact of the unrealistic model that was analyzed. On the real vehicle these stresses will be distributed by a large weld bead, rather than concentrated at the thin joint in our solid model. However, because this joint carries the majority of the load, it is subject to numerous loading and unloading cycles as the vehicle absorbs bumps and vibrations. Fatigue failure, a problem we have experienced in the past, is a serious concern. Accordingly, we will be adding a thin sheet metal gusset across the joint to distribute the load and reduce the potential for fatigue failure at this critical joint. Overall, our analysis indicates no major points of concern for the structural integrity of our vehicle frame, even under loading conditions far exceeding anything we expect to see during riding. We will be mitigating any potential for fatigue issues with some minor sheet metal bracing.

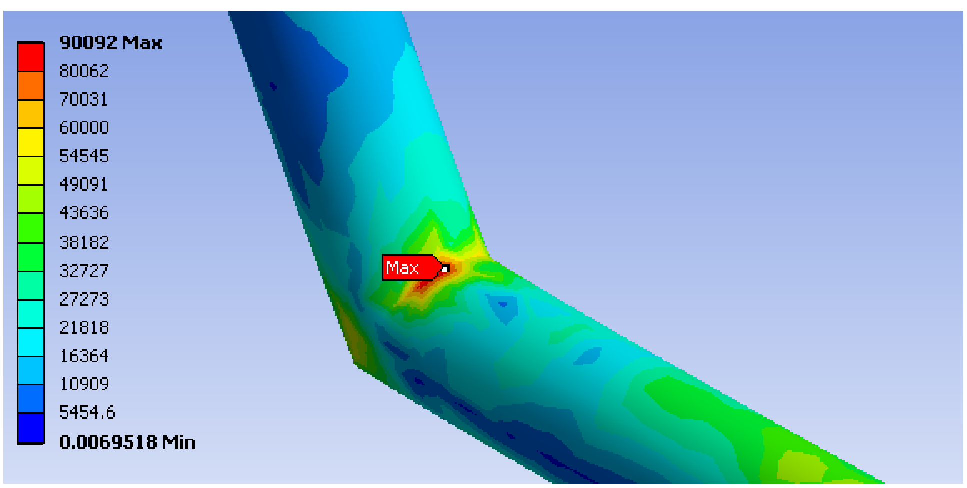

Figure 13: Close-up of the main frame joint – Note the small region where predicted equivalent stress exceeds yield stress of 60ksi (stress values given in psi).

Fairing Analysis

We utilized SolidWorks Flow Simulation to perform computational fluid dynamic analysis on our fairing design. Our analysis enables comparison to previous competition vehicles through surface pressure and fluid velocity plots. We assumed an 18m/s wind speed (~40mph) and a 200µm roughness of the fairing outer surface for the analysis. To simplify the model and improve computational speed, drag added by the wheels was neglected.

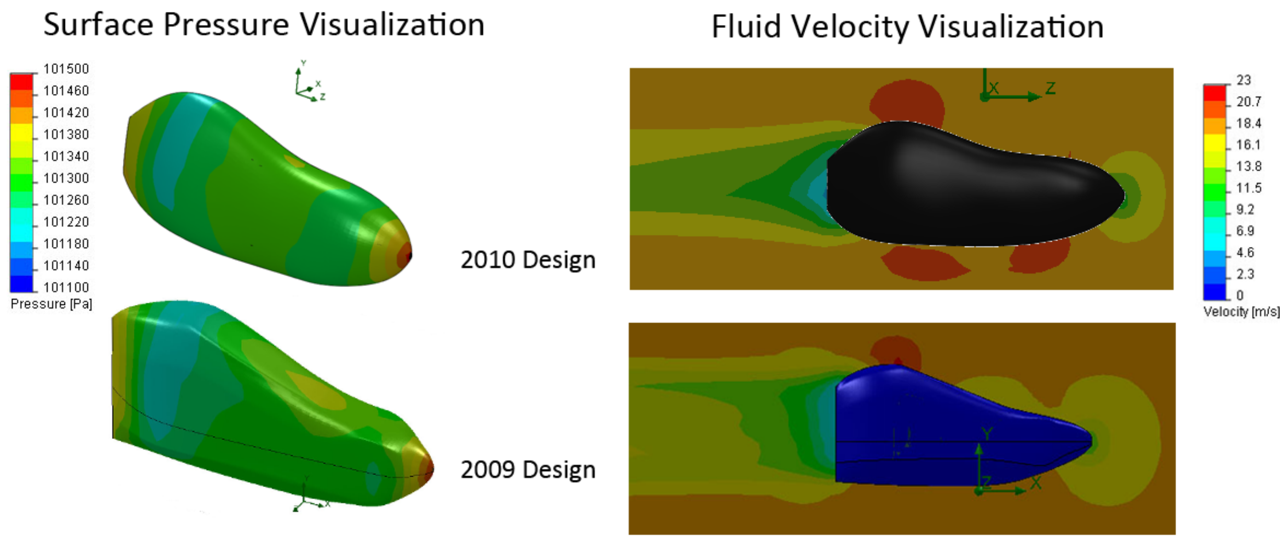

Figure 14. Surface pressure and fluid velocity visualization – Note that the surface pressure for the current fairing is more uniform than the previous year. Fluid velocity varies similarly.

Our optimized fairing design for *Bucephalus* shows similarities to last year's final concept. As seen in Figure 14, the surface pressure visualization shows a high pressure zone at the nose of the fairing and a low pressure area on the tallest section. These values are expected given the concavity changes in the fairing geometry. Overall pressure varies from 101100Pa to 101500Pa for both fairings as a result of their similar characteristic shape.

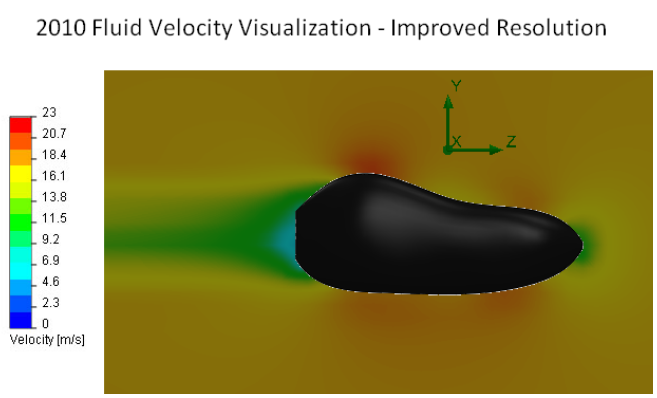

Figure 15: Fluid velocity visualization for 2010 design – Note that the large high velocity areas present under the fairing on the comparison diagram are much less noticeable.

Fluid velocity for both fairings follows the same general trend. Low velocity regions exist at the front and rear sections of the fairing, where the flow converges and diverges. Both fairings display a high velocity zone at the top of the canopy where the frontal area is the largest. Per Figure 14, the 2010 design exhibits two high velocity areas under the fairing. These anomalies are only artifacts of the color scheme; the velocity profile is actually well distributed under the fairing (Figure 15).

Our primary concern in fairing design is low drag force. Drag force is a function of both fluid and geometric parameters [7],

$$F_D = \frac{1}{2}\rho C_d A v^2$$

where ρ is air density (1.184kg/m^3) [6] and v is air velocity (18m/s) in the vehicle reference frame. However, C_dA is purely dependent on fairing geometry and thus serves as a quantitative metric for fairing comparison. Table 3 shows the computed C_dA values for our vehicles over the past four years. This year our C_dA approaches *Vega*, our competition bike from two years ago. However, *Vega's* aerodynamic advantage comes from its much lower frontal area and heavily reclined rider position, making the vehicle difficult to ride.

Vehicle	Drag Force (N)	C_dA (m^2)
Aurora	6.13	.046
Vega	3.98	.021
Helios	6.11	.032
Bucephalus	4.19	.022

Table 3: Drag forces and C_dA values for *Bucephalus* and previous vehicles – Our current competition vehicle has a similar C_dA to a vehicle of much smaller frontal area (vehicles ordered oldest to newest).

In addition to a 4.19N drag force, our CFD also predicts a 1.2N downforce. While high downforce enhances vehicle handling at high speeds by keeping both wheels in contact with the racing surface, 1.2N is unfortunately negligible in comparison to vehicle and rider weight. Optimizing downforce was therefore secondary in our fairing design criteria. Overall, the fairing design compares favorably to the design from previous years, confirming the merit of our design process.

Roll Bar Analysis

According to the competition rules we must show, both through analysis and testing, that the roll bar can withstand two types of loading conditions. Using SolidWorks' embedded finite element analysis tool, the initial roll bar design was analyzed and refined. As described in the Roll Bar Design section, the roll bar's material, geometry, and placement on frame were dictated to meet certain criteria. We considered rider size, ease of rider entry/exit, and interaction with the fairing.

We modeled the entire frame of our vehicle, shown in Figure 16, as a set of beam elements. The beam elements model each frame and roll bar member as a two dimensional member with structural properties specified by the frame material and tube cross section. This simplification is necessary due to limitations on model size in our analysis packages. We bolster these simplified simulations with more detailed shell element analysis for localized regions.

The first load condition specified by the competition rules is a top load of 600lbf applied at 12° from vertical towards the rear. Within SolidWorks Simulation this load was applied as a distributed load across the top roll bar member. The modeled frame was constrained by the base of the head tube and by the rear dropouts. The front constraint at the head tube was fully constrained in translation and unconstrained in rotation. Similarly, the rear dropouts were constrained in translation in all directions except along the long axis of the frame. Figure 16 shows the von Mises stresses across the frame and roll bar under the top load condition.

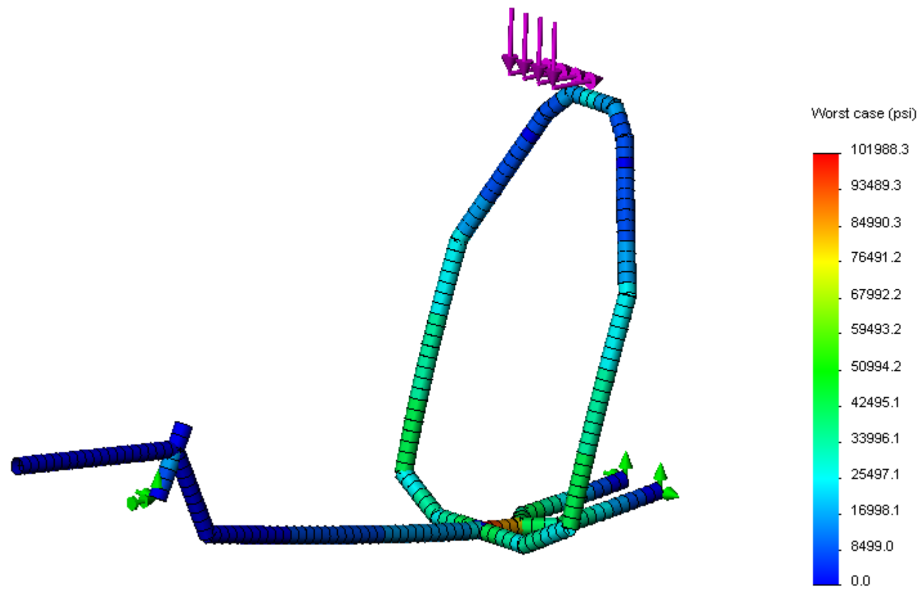

Figure 16: Initial roll bar geometry and frame under top load condition – Note the extreme stress concentration where the roll bar joins the frame.

Initial analysis of the proposed roll bar geometry showed stress concentrations around the main joint with the frame. The maximum equivalent stress predicted by the analysis was in excess of 100ksi, a serious concern given that our frame material, 4130 Steel, yields around 60ksi. In order to investigate the stress concentration around the joint, the bottom members of the roll bar and a section of the frame were modeled in ANSYS, equivalent loads were applied to the ends of the roll bar members, and the ends of the frame tube were suitably constrained in translation. Figure 17 shows the results of this analysis and highlights the need for bracing or other modifications to the proposed roll bar, due to the regions of high stress approaching the yield stress of our material, 60ksi, including unseen regions on the interior of both the frame and roll bar members.

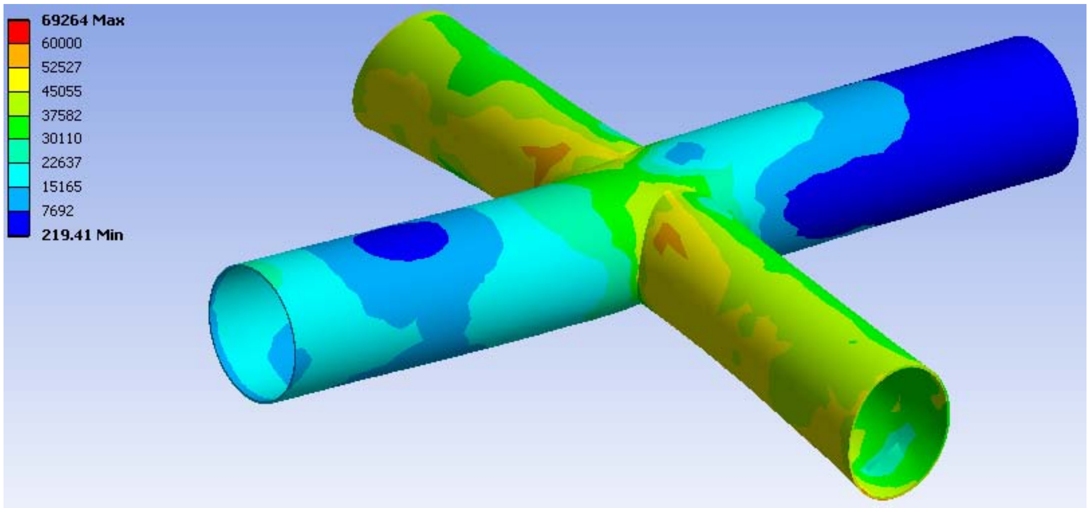

Figure 17: Close-up of joint between roll bar and frame – Note stress concentrations in excess of material yield stress (stress values given in psi).

Several variations on the proposed roll bar design were modeled and tested, involving minor alterations to the location of the roll bar on the frame, its angle with respect to the frame, or the addition of support members. We concluded that, as expected, simply shifting the location of the roll bar shifts the stress concentration but does not reduce it. Modifying the angle of the roll bar with respect to the frame is an appropriate way to reduce stress at the frame joint, as the initial design mounted the roll bar perpendicularly to the frame giving it a 4° rearward tilt. This angle magnifies the effects of the top load, increasing the moment applied about the frame joint. By tilting the roll bar forward we found we could reduce the stress concentration at the frame joint; however, manufacturing and rider entry/exit concerns prevent this from being a viable option. This left the addition of support members to the current roll bar geometry as our only option.

Several different locations and tube sizes were analyzed for potential roll bar supports, eventually settling on 0.5in diameter tube of the same wall thickness and material as the rest of the frame. These supports brace the vertical members of the roll bar to the rear fork. Design for manufacturing considerations drove selection of a particular variation of this design. The ease of positioning and welding of the support members is significantly increased by providing a bracket or other suitably constraining location for the ends of the members. By moving the joint with the rear fork out to the dropouts, we were able to provide an improved welding location on top of our existing custom dropouts at the rear. Figure 18 shows the equivalent stress distribution of the final roll bar design under the top load condition. Analysis predicted maximum total deformation of the top member of the roll bar to be 0.231in. Larger support members were modeled and analyzed but they provided little gain in terms of further reduction in equivalent stresses around critical joints on the roll bar.

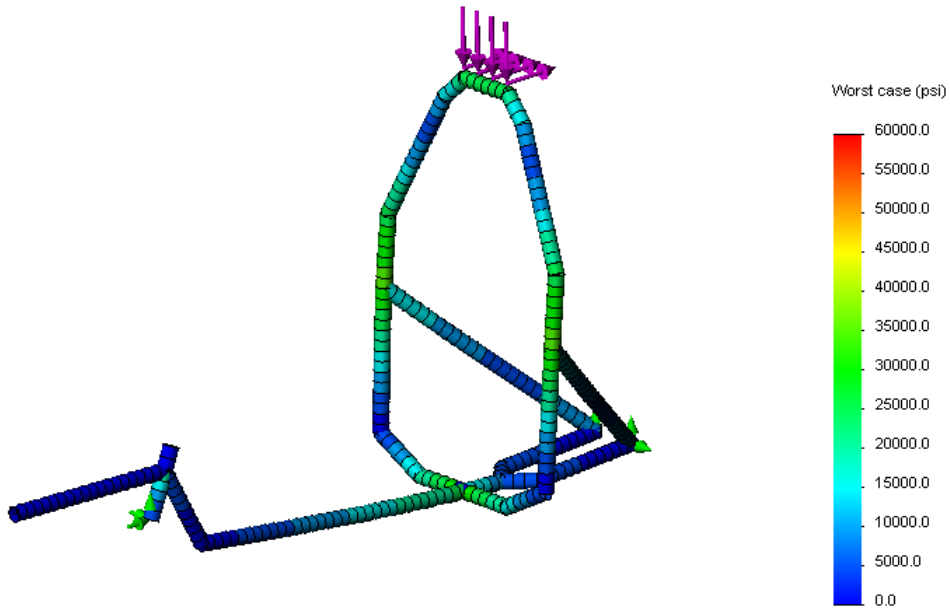

Figure 18: Equivalent stress results for final roll bar iteration – The final roll bar successfully passes analytical vertical load testing.

The competition specifies a side load condition of 300lbf applied to the roll bar "at shoulder height". The difficulty with this load condition comes in applying the proper constraints to the frame to accurately model how a load of this type might be applied in a rollover crash. Using the same constraints as the top load condition (constraints only in translation) is inappropriate because it locks the front and rear forks, and therefore the wheels, from rotation and twists the whole vehicle about the rear axle. However, in such a shoulder-high side impact from a rollover crash, the wheels must be off the ground and would be completely unconstrained.

Because of the potential for stress concentrations around the roll bar, we chose to analyze the roll bar for side loading as a shell element model, which approached the size limitations of our analysis package. Fixing the node at the joint between the roll bar and the frame in both translation and rotation provides the most realistic constraint, modeling the deformation of the roll bar relative to the frame, but this was found unworkable in actual testing. Instead, we chose to test compression of the roll bar, as shown in Figure 19. This loading consisted of applying a force to the roll bar as shown by the black arrow, while constraining the opposite member of the roll bar in translation, except for one end free to translate axially. Maximum predicted deformation of the roll bar in this case is 0.069in, and all von Mises stresses are well below the yield strength of the steel.

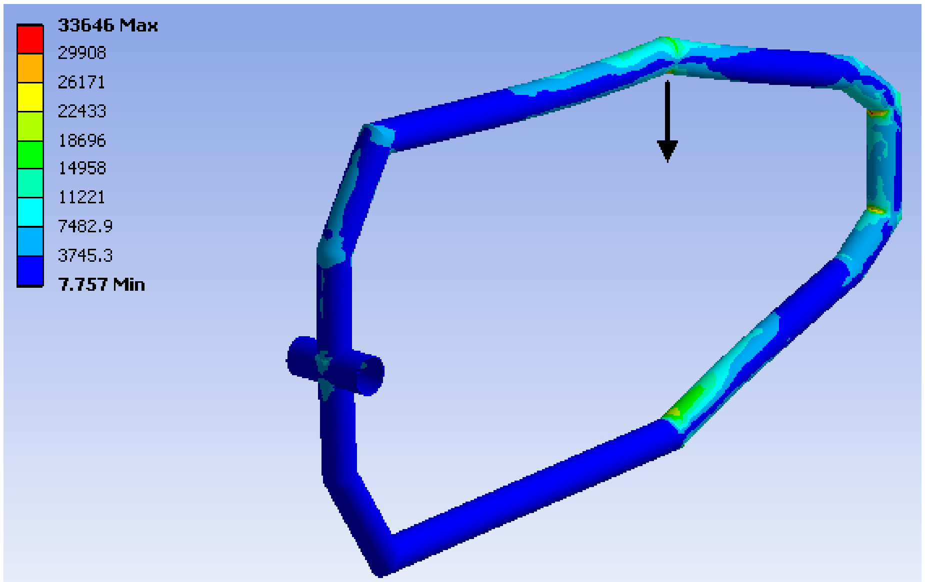

Figure 19: Equivalent stress distribution across final roll bar design under 300lbf side load being applied as shown by black arrow.

Cost Analysis

Single Vehicle Cost Estimation				
Description	*Quantity*	*Unit Cost*	*Units*	*Total*
Frame				
Thin Walled 4130 Steel Tubing	9	$7.20	Per Foot	$64.80
Welding Supplies	1	$20	Lump Sum	$20.00
4' x 8' Sheet, Plywood	1	$20	Per Board	$20.00
Aluminum Blocks	1	$30	Lump Sum	$30.00
Assorted Hardware	1	$60	Lump Sum	$60.00
			Subtotal	**$194.80**
Fairing				
Epoxy	10	$60	Per Gallon	$600.00
Fiberglass, 6 oz.	22	$25	Per Yard	$550.00
Assorted Composites Tools	1	$50	Lump Sum	$50.00
Weather Balloon	2	$20	Per Balloon	$40.00
Fabric	10	$1.99	Per Yard	$19.90
Sewing Supplies	1	$10	Lump Sum	$10.00
PETG (4' x 8')	0.25	$70.90	Per Sheet	$17.73
Coroplast (4' x 8')	0.25	$20.00	Per Sheet	$5.00
			Subtotal	**$1,292.63**
Drivetrain				
Derailer	1	$100	Per Unit	$100.00
Wheels	2	$100	Per Wheel	$200.00

Front Crankset	1	$50	Per Unit	$50.00
Chains	2	$20	Per Unit	$40.00
Interchange Sprockets	2	$15	Per Unit	$30.00
Pedals	1	$75	Per Set	$75.00
Brakes	1	$50	Per Set	$50.00
			Subtotal	**$545.00**
Seat				
Plywood	1	$10	Per Board	$10.00
Stain	1	$5	Per Can	$4.97
Wood Screws	1	$10	Per Box	$10.00
1/8" Steel Plate (6" x 2')	1	$30	Per Plate	$30.00
Aluminum Block	1	$20	Per Block	$20.00
Pins	2	$2	Per Pin	$4.00
Sanding Supplies	1	$5	Lump Sum	$5.00
			Subtotal	**$83.97**
			Total Cost	**$2,116.40**

Table 4: Cost Estimate for Single Vehicle.

Production Vehicle Cost Estimation				
Description	*Quantity*	*Unit Cost*	*Units*	*Total*
Labor				
Machinist/Welder	1	$ 4,000.00	Per Month	$4,000
Composite Technician	1	$ 5,000.00	Per Month	$5,000
Manager	1	$ 5,000.00	Per Month	$5,000
			Labor Total	**$14,000**
Bike Costs				
Cost Savings Factor for Bulk Purchase	---	0.5		
Frame Jig	1	$25	Lump Sum	$25
Drivetrain Components	10	$272.50	Per Bike	$2,725
Frame	10	$72.40	Per Bike	$724
Fairing	10	$646.31	Per Bike	$6,463
Seat	10	$41.99	Per Bike	$420
			Parts Total	**$10,357**
			Total Cost	**$24,357**
			Cost Per Bike	**$2,435.70**

Table 5: Cost Estimate for 10 Vehicle Production Run. Note that the cost savings factor is applied to all components.

Testing

Developmental Testing

Frame/Drivetrain Testing

We built a functional prototype to explore and evaluate possible designs for inclusion in the final race vehicle. The prototype allowed us to see how new concepts would work in practice and allowed riders to begin to familiarize themselves with the vehicle. The main system we evaluated on the prototype was a new steering design. Secondarily, we tested and validated the front wheel drivetrain design. Riders also provided qualitative feedback on the prototype's ridability and overall comfort.

As covered previously, our prototype's innovations center on the new steering design. We selected a main tube height of nine inches, mounting the steering under it. Overall, testing proved the steering design a success. Riders of all heights felt that the new design was easy to control and an improvement over the old design, which short riders often found uncomfortable and could interfere with the legs of tall riders. A few alterations were made to the steering mechanism to improve overall vehicle aerodynamics and steering reliability, but prototype testing confirmed the merits of our ideas.

Even though prototype design proved sound, testing revealed a few problems. One issue was bicycle stability. Our low seat angle resulted in poor balancing ability. The rider was not as able to feel the bike out of balance as a result of the low seat angle; once out of balance it became difficult to correct. Also, we found that the pedal path interfered with the front wheel while turning. This was solved by switching from a 20in to a 16in wheel. Finally, we had problems with the steering connection between the handlebars and the bottom bracket. The steering exhibited off-axis wobble, as the connection to the taper of the bottom bracket did not completely constrain the handlebars (Figure 20). We manufactured the prototype connection out of 1/4in steel; we used a bicycle-specific component for the final vehicle.

Figure 20: Prototype (left) and Competition (right) vehicle steering mechanisms – Each steering connection to the bottom bracket cartridge is circled and the bottom bracket for each one is labeled. Note that the competition vehicle has a modified drive-side crank for connection, while the prototype connects the handlebars via 1/4in steel plate.

Our front wheel drive design proved successful through testing. Through riding and static testing, we found that we encountered fewer chain problems than with previous designs. As a result of our testing and observations, we decided to go ahead with front wheel drive for the final vehicle. To minimize derailments, we attached chain guards to the competition vehicle as detailed in the Drivetrain Design section. The addition of these Teflon members nearly eliminated chain derailments all together.

Accelerometer Testing

In order to experimentally validate the parameters used in our finite-element analysis, we tested the dynamic acceleration at different points along the frame as the rider traveled over a bump. In the past we have assumed a worst case acceleration of three times the acceleration of gravity ($3g$'s or 29.4m/s^2) (Carroll, 2003) in the z or vertical axis (see coordinate definition in Figure 21) to determine the worst case load condition for analysis of our frame.

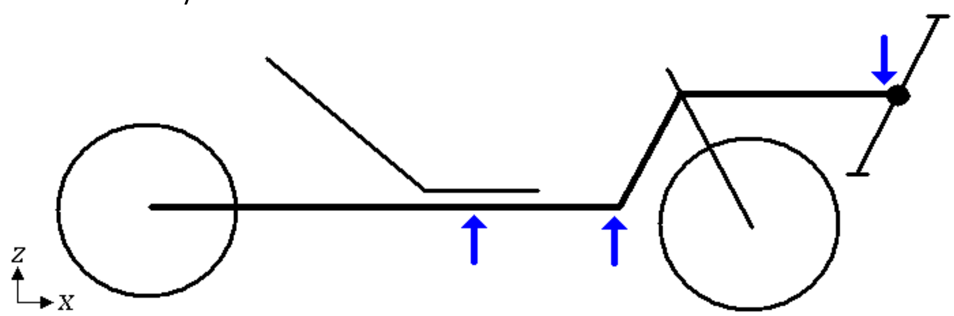

Figure 21: Accelerometer locations – Data were gathered at the locations identified by the blue arrows.

To test this assumption we used a single axis accelerometer mounted to the vehicle frame and collected data with a data acquisition unit and a laptop. For our test, we drilled holes in the prototype frame at three positions to serve as rigid attachment points for the accelerometer: at the bottom bracket, the lowest joint, and underneath the seat (as shown in Figure 21).

To simulate a bump that might be encountered during the course of riding, the rider rode the vehicle over a metal pipe in two separate trials. The first trial used a 0.75in diameter pipe and the second used a 1.25in diameter pipe. The rider began from rest at a fixed distance from the bump (approximately 50ft) and accelerated, reaching approximately 15mph at the point of first contact with the bump. We found that after just a few practice runs, the rider could repeatedly reach the same speed (plus or minus 2mph). The test was conducted indoors on a smooth surface to minimize noise. Data was collected continuously before, during, and after the rider rode over the bump in both the frequency and time domains. Two trials were conducted for each accelerometer position and pipe size combination to ensure data precision.

As expected, the observed accelerations were higher for the larger bump regardless of sensor placement. As shown in Figure 22, the first, higher set of peaks corresponds to the front wheel impact and the second, lower set of peaks to the rear wheel impact. For both pipe sizes the acceleration was highest at the bottom bracket due to high elasticity of the frame supporting the bottom bracket and the larger distance traveled by that point compared to the rest of the frame when the front wheel hits a bump. At the joint the accelerations were approximately twice those observed under the seat.

The accelerometer location under the seat gives the most accurate estimation of the acceleration of the rider due to the bump because it is mounted directly below the rider's center of gravity. The maximum value observed during our testing at this location was approximately 2.5m/s^2 or $0.25g$'s. This value was observed with a 1.25in bump. This value is one-twelfth of our $3g$ maximum acceleration assumption. As a result of this testing we believe this assumption to be an extreme upper bound for the accelerations we expect to encounter during casual riding and racing of our vehicle and therefore adequate as a worst case condition for analysis purposes.

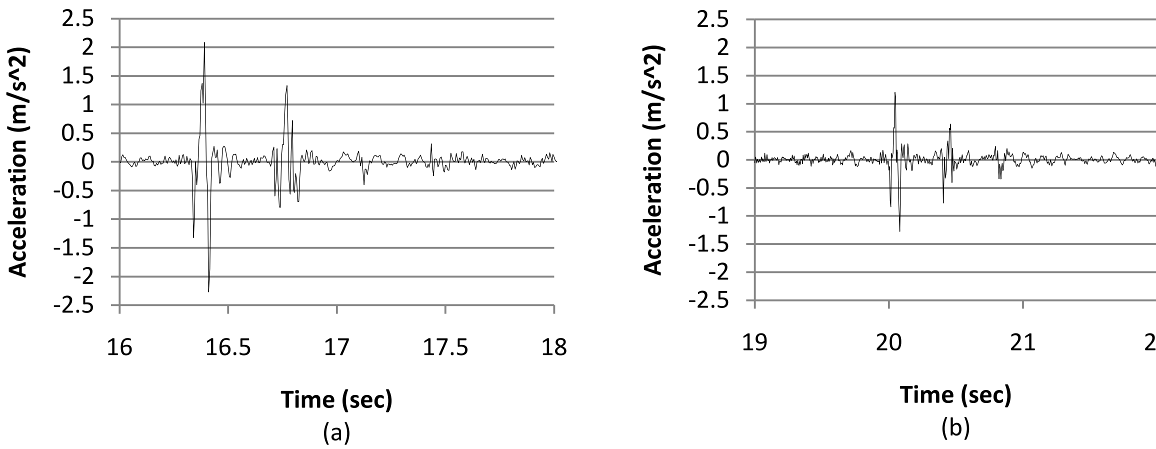

Figure 22: Acceleration results – Data from under the seat for the a) 1.25in bump and the b) 0.75in bump.

Fairing Fabrication Testing

Before building the fairing with our new mold technique, we experimented with the technique during two test layups. First, a few team members made a snow cannon cowling for a class project (Figure 23a). The cowling was a 2-ft diameter cylinder of a comparable length to the fairing. In this initial test, we decided to not use mold release; instead, we used a felt "sock" as a structural component under the fiberglass. The epoxy-soaked felt made the cowling stiff and brittle after removal from the mold, making shape alteration impossible. We chose felt as our fabric because it deforms equally in all directions; however, it easily experienced plastic deformation and made the cowling wider than intended.

Figure 23: Mold Testing Examples – (a) A snow cannon cowling, using a felt fabric composite and (b) Scale model of last year's nosecone with ribbing structure for increased rigidity.

As a second test, we made a 1:2 scaled copy of last year's nosecone (Figure 23b). Here, we used a 3-ft weather balloon and stronger cotton fabric. We only laid up a single layer of fiberglass and used saran-wrap mold release, so the final shape was flexible and could be squeezed into the proper cross-sectional geometry. We also tested our ribbing technique, using Coroplast strips to reinforce the nosecone against hoop and axial stresses.

As a result of this testing, we determined that the inflatable mold technique was a labor efficient replacement for a foam mold, while producing a better product than last year's cardboard ribbed mold. We also became confident in our fabric choice, weather balloon handling technique, mold release, and ribbing patterns. The primary lesson learned was the importance of using only a thin layer of fiberglass on the inflated mold. After the lay-up, an outer scaffolding was used to correct the shape with ribbing.

Performance Testing

Drivetrain Efficiency

After using rear-wheel drive for both the prototype and the competition bikes last year, we wanted to re-evaluate the option of using front wheel drive to avoid routing a chain around the below-seat steering assembly. Drive train efficiency was one of our primary concerns in such a design change.

We first mounted the bicycle so that the drive wheel was resting on the rotating disc of a dynamo-motor assembly (Figure 24). We drove the motor at a fixed voltage to ensure consistency between trials. The dynamo was used to measure the angular velocity of the wheel. We then removed the bicycle and drove the dynamo at the chosen voltage again, adjusting the dynamo brake until the angular velocity was the same as when the bicycle was resting on the motor. The brake torque gave us the frictional torque of the drivetrain at the given RPM.

Figure 24: Our drivetrain efficiency testing setup – This test apparatus provides an accurate approximation to actual riding conditions.

The pedal velocity generated is constant and similar to that of a rider; it is between .65 and 1.8rps. Also, by using the friction of the motor shaft against the wheel of the bicycle to run the drivetrain, we incorporated efficiency losses due to the tire's interaction with the ground. Our chief assumption is that the drivetrain efficiency is the same if it is driven from the wheel, rather than the pedals. While this is likely not true, we mitigated this assumption somewhat by running the drivetrain rotationally backwards, ensuring that the tension and slack sides of the chain remained consistent.

Gear Ratio	Disc RPM	Torque Loss (oz-in)	Power Loss (W)	Pedal RPM	Efficiency (%)
Bucephalus 2010 (FWD)					
4.55:1	880	30.4	19.78	77.36	**93.06**
6.83:1	887	21.9	14.36	51.99	**94.96**
9.01:1	890	16.9	11.12	39.12	**96.10**
Prototype 2010 (FWD)					
5.54:1	889	17.5	11.50	64.16	**95.96**
7.13:1	880	28.5	18.55	49.40	**93.49**
Helios 2009 (RWD)					
4.81:1	884	24.5	16.02	58.00	**94.38**
7.44:1	887	19.0	12.46	37.66	**95.63**
Prototype 2009 (RWD)					
2.49:1	883	18.5	12.08	111.92	**95.76**

Table 6: Drivetrain Efficiency Test Results – Given a variety of gear ratios on a range of vehicles.

Given the distribution of efficiency data from our 2010 prototype vehicle as shown in Table 6, we concluded that the front wheel drivetrain would only decrease our efficiency by about 1.5%, which is clearly dwarfed by aerodynamic efficiency losses. Our competition vehicle shows similar efficiency after fabrication, even over a wide range of gears.

Maneuverability Testing

Given our current number of vehicles in working condition, we performed a comparative study to test rider comfort on *Bucephalus*. Several of our design changes since the prototype, such as the new steering system, adjustable seat angle, and roll bar position, had the potential to affect rider ergonomics and vehicle stability. We built a small slalom course of eleven cones spaced 10ft apart and measured the number of cones each rider was able to successfully complete before losing control.

Cones Successfully Maneuvered

VEHICLE	AVERAGE
Bucephalus	89%
Prototype	92%
Helios	96%

Figure 25. Maneuverability testing on a slalom course – Note similar performance of all vehicles.

The average rider scores were remarkably similar across our three vehicles, well within the accuracy margin of this experiment (Figure 25). There was a slight tendency for riders to perform better on older vehicles. *Bucephalus* has only been ridable for a few weeks, while last year's *Helios* has been a staple vehicle for grocery store trips since the last HPVC. We are confident that *Bucephalus*'s lower rider comfort will be alleviated within the coming weeks before HPVC, and do not plan any substantial design changes to increase vehicle stability. This testing has confirmed that *Bucephalus* has maneuverability on par with previously successful vehicles.

In addition to maneuverability testing, we made a simulated endurance event around the campus on our three vehicles to practice rider swaps, judge rider comfort, and troubleshoot mechanical endurance problems. Riders were easily comfortable with racetrack geometry similar to the competition track, including making sharp turns and accelerating down straightaways. Aside from one misaligned chain guide, technicians servicing *Bucephalus* needed only adjust the seat for various riders through two hours of racing.

Roll Bar Testing

As per ASME safety rules, we performed load testing on the final roll bar in addition to pre-fabrication analysis. We do have a small Instron tensile tester available to us, but loading the vehicle into the test apparatus is impossible. Our alternative method consists of loading the roll bar with weights by hand. The FEA predicted a 0.231in maximum displacement of the roll bar under top loading, and a 0.069in displacement under side loading. While we could not obtain accurate total displacement data from this setup, our visual inspection of the roll bar during loading was consistent with these measurements.

Figure 26: Vertical load testing – 600lbf was suspended 12° from vertical. The roll bar successfully passed the loading test and only displaced elastically under load. The two team members pictured are only applying small horizontal forces to balance the vehicle.

To load the roll bar vertically, we tilted the bike until the wheelbase was 12° off the horizontal, then placed 600lbf on a platform suspended from the top of the roll bar (Figure 26). The roll bar expanded at the corners and tilted backwards, but both displacements were well under an inch, verifying our computational results. The roll bar under loading did not interfere with the rider. After loading, the roll bar returned to its original shape, indicating that the deformation was within the elastic region of the steel.

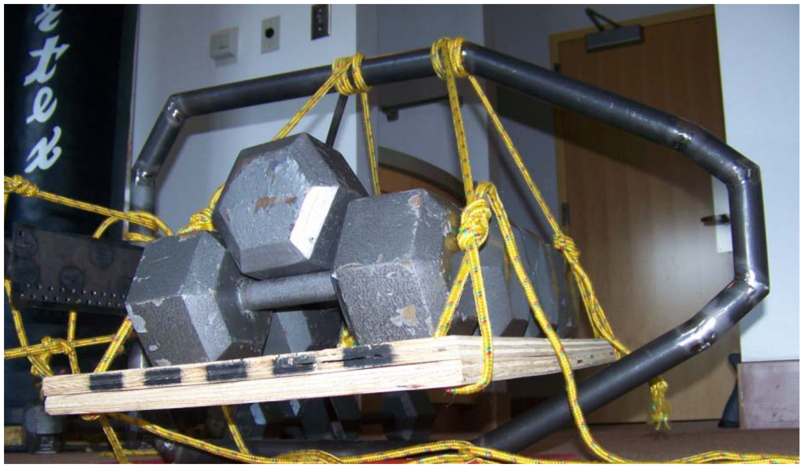

Figure 27: Horizontal load testing; 300lbf were suspended at shoulder height. The roll bar again passed the loading test and only displaced elastically under load.

Our horizontal test consisted of placing the bike on its side and hanging 300lbf from the side of the roll bar (Figure 27). The roll bar did not displace noticeably under load, and maintained its original shape after the unloading. These results are consistent with the predicted 0.069in displacement.

Safety

Roll Over Protection: The roll bar has been attached and tested as specified by the 2010 HPVC guidelines and all riders fit within the roll bar while wearing a helmet. Before construction, we used a cardboard prototype to ensure that all riders fit comfortably within the roll bar. Upon discovering that some of our measurements had been inaccurate, we widened the roll bar by one inch at that point. According to our load testing, our manufactured roll bar deforms much less than an inch which ensures that our roll bar will not impact the rider in a crash. Initially, there was some concern that the steering, which is located below the roll bar, would put riders' hands at risk for abrasion and injury. We intend to reinforce the fairing around the steering mechanism and add padding to protect riders' hands.

Seat Belt: We are using an automotive-quality four-point harness. It is a commercial product in excellent condition and is structurally attached to the vehicle.

Steering System: The steering is structurally attached via a modified crank arm to a bottom bracket welded into the frame to minimize off-axis play. In testing, we have found the steering geometry to be suitably ergonomic and to provide adequate control of the vehicle. With additional practice, rider skill in maneuvering will continue to improve.

Vehicle Hazards: All sharp edges have been deburred and open tube ends have been eliminated. We identified a potential hazard where the front chain ran close to the rider's legs. This hazard has been eliminated by moving the chain path closer to the vehicle to allow more space for the rider. In addition, by using Saran wrap as a mold release, we have ensured a smooth interior fairing finish so there are no exposed fiberglass hazards.

Field of View: The fairing is still in the process of fabrication. However, we intend to install a clear PETG plastic window that will give the rider a full field of view from both sides of the vehicle. We are also making a special effort to avoid deforming the window in any way that impedes visibility. Therefore, we intend to cold bend our plastic in one dimension rather than using thermoforming methods.

Hardware: We have mounted front wheel brakes, used bicycle-specific components, and employed lock nuts wherever possible.

Drivetrain Reliability: We have designed our drivetrain to operate safely on a variety of adverse road surfaces and riding conditions. Chain guides, proper chain tensioning, and many hours of real world testing have produced our safest and most reliable drivetrain to date.

Bibliography

[1] Brown, Sheldon, et al. Harris Cyclery Articles [Online]. Accessed: 9 March 2010. http://sheldonbrown.com/articles.html.

[2] Carroll, Douglas R. 2003. *The Winning Solar Car.* Warrendale PA : SAE International, 2003.

[3] Personal Interview. Brian Rondo (Hamel Brothers Auto Repair). Lowell, MA, October 28, 2009.

[4] Personal Interview. Rob Vandemark (Seven Cycles). Watertown MA, January 26, 2009.

[5] Smith, Carroll. *Engineer to Win*. Osceola WI : Motor Books, 1985.

[6] Wikipedia. Density of Air [Online]. Accessed: 12 March 2010. http://en.wikipedia.org/wiki/Density_of_air.

[7] —. Drag Equation [Online]. Accessed: 12 March 2010. http://en.wikipedia.org/wiki/Drag_equation.

[8] Wilson, David Gordon. *Bicycling Science.* Cambridge : The MIT Press, 2004.

2010 Human Powered Vehicle Challenge East
Sponsored by ASME and Central Connecticut State University (CCSU)

Form 6: Vehicle Description
Due April 5, 2010

(Dimensions in inches, pounds)

Competition Location: New Britain, CT

School name: Central Connecticut State University

Vehicle name: Bucephalus

Vehicle number 3

Vehicle type Unrestricted_______ Speed___X____

Vehicle configuration

Upright ______ Semi-recumbent X

Prone ______ Other (specify) ________________

Frame material 4130 Chro-moly Steel

Fairing material(s) Fiberglass, Coroplast

Number of wheels 2

Vehicle Dimensions

Length 83in Width 22in

Height 42in Wheelbase 53in

Weight Distribution Front 60% Rear 40% Total N/A*

Wheel Size Front 16” Rear 20”

Frontal area 750 in^2

Steering Front X Rear ______

Braking Front X Rear ______ Both ______

Estimated Cd .045

Vehicle history (e.g., has it competed before? where? when?)

Our vehicle has not competed this year at any competitions.

*Fairing is not completed, so final weight is not yet available